

Characterization of Initiation and Growth of Selected Severe Convective Storms over Central Europe with MSG-SEVIRI

FABIAN SENF

Atmospheric Dynamics and Predictability Branch, Hans Ertel Centre for Weather Research, Leibniz Institute for Tropospheric Research, Leipzig, Germany

FELIX DIETZSCH

Deutscher Wetterdienst, Offenbach, Germany

ANJA HÜNERBEIN AND HARTWIG DENEKE

Leibniz Institute for Tropospheric Research, Leipzig, Germany

(Manuscript received 16 June 2014, in final form 8 October 2014)

ABSTRACT

The early development of severe convective storms over central Europe was investigated on the basis of nine cases from 2012. Using data from the Spinning Enhanced Visible and Infrared Imager (SEVIRI) imaging radiometer aboard a geostationary Meteosat Second Generation (MSG) satellite, dynamical and microphysical properties of developing storms were monitored and combined. Several satellite-based storm properties, for example, cloud-top temperature, cloud-top cooling rate, and cloud particle effective radius, were investigated following the storm tracks. A framework for quantification of uncertainties of along-track properties resulting from tracking errors was also introduced. The majority of studied storms show a distinct maximum in cloud-top cooling rate; the corresponding time was used for track synchronization. The cloud growth phase was divided into an initial updraft intensification period before the maximum cooling and a continued growth period afterward. The initial updraft intensification period is variable and strongly depends on the convection initiation mechanism and detection conditions. The continued growth period is more confined, lasting between 30 and 45 min. The change in anvil size and the resulting average anvil edge velocity were determined from infrared satellite images. As a consequence of mass transport, the anvil edge velocity shows its highest correlation with the cloud-top vertical velocity approximately 20–30 min after the maximum in the cloud-top cooling rate. Larger effective radii of ice crystals were observed for vertically slower-growing clouds. The largest anticorrelation between cloud-top vertical velocity and effective radius was found at a time lag of 20 min after the maximum in cloud-top cooling.

1. Introduction

Observations from geostationary satellites have been used since the 1970s for the characterization of the development of thunderstorms (Adler and Fenn 1979a,b; Heymsfield et al. 1983). Observational capabilities of meteorological satellite imaging have heavily improved since then. Spanning the complete globe with spatial resolutions down to 3 km and repeat cycles of 5 min and less (Schmetz et al. 2002; Schmit et al. 2005), satellite

images have become indispensable tools for the monitoring and characterization of deep moist convection.

The rapid cooling of cloud tops can be seen in the thermal radiation of the growing clouds, which indicates the release of convective available potential energy by developing convection. The cloud-top cooling (CTC) as a measure of vertical cloud growth has recently been incorporated in satellite-based convection-initiation detection algorithms (Roberts and Rutledge 2003; Mecikalski and Bedka 2006; Zinner et al. 2008; Mecikalski et al. 2010a,b; Siewert et al. 2010; Sieglaff et al. 2011; Merk and Zinner 2013; Sieglaff et al. 2014). It has been shown that detailed knowledge about the growth phase of developing storms increases predictive skill of nowcasting

Corresponding author address: Fabian Senf, Leibniz Institute for Tropospheric Research, Permoserstraße 15, 04318 Leipzig, Germany.
E-mail: senf@tropos.de

applications. For instance, satellite-based cloud-top cooling rates were used by [Roberts and Rutledge \(2003\)](#) to quantify cloud growth in the vicinity of radar-derived boundary layer convergence features in the United States. They demonstrated that cloud growth rates from satellite contain important precursor information to storm initiation, potentially providing up to 30 min of advance notice of storm initiation defined by radar reflectivities greater than 35 dBZ. In addition, [Mecikalski et al. \(2008\)](#) and [Walker et al. \(2012\)](#) reported average nowcast lead times of 30 min with extremes reaching up to 2 h for early detection of convective events defined in a similar way as in [Roberts and Rutledge \(2003\)](#).

Apart from the nowcasting aspect, it is also important to collect information for improving our basic understanding of dynamical and microphysical processes in developing storms, for instance, in support of cloud modeling. Storm life cycles have been recorded in several ways using a variety of approaches to get a synchronized picture of storm evolution. For instance, [Mecikalski et al. \(2011\)](#) analyzed developing storms across Europe and synchronized their tracks according to the time when the cumulus clouds are deepest. They found that derived cloud properties provide additional insights into the dynamical and microphysical state of growing cumulus clouds. Changes in the cloud optical thickness are related to changes in the vertical cloud extent, and changes in cloud particle effective radius are connected to updraft strength and glaciation and indirectly to precipitation formation processes. Furthermore, [Matthee and Mecikalski \(2013\)](#) studied the relation between thermal storm properties and lightning in equatorial Africa. They used the time of the first lightning stroke and maximum volume of reflectivity values above 35 dBZ for synchronization of storm tracks for lightning-producing and nonlightning storms, respectively.

Satellite-observed anvil expansion rates provide, in addition to cloud-top cooling rates, information about cloud growth processes. They have been related to further development of convective systems and severe-weather phenomena ([Adler and Fenn 1979a](#); [McAnelly and Cotton 1989](#); [Machado et al. 1998](#); [Machado and Laurent 2004](#)). [Machado et al. \(1998\)](#) as well as [Machado and Laurent \(2004\)](#) successfully predicted the typical life cycle of mesoscale convective systems in South America on the basis of knowledge of the initial expansion. They demonstrated that large initial expansion rates can lead to increased lifetimes of convective systems and that the maximum area expansion occurs close to the time at which maximum precipitation is recorded.

Thunderstorms with a higher degree of severity also attain greater growth rates during their vertical expansion (e.g., [Adler and Fenn 1979a,b](#); [Reynolds 1980](#); [Heymsfield et al. 1983](#), and many others). In a more

recent study, [Cintineo et al. \(2013\)](#) investigated cloud properties, including optical properties such as cloud optical thickness and effective radius, for severe versus nonsevere storms in the United States. They discussed that the rate of change in top-of-troposphere infrared emissivity and in ice fraction is typically more than 2 times as large for severe as for nonsevere thunderstorms. They also investigated the trend in cloud anvil area marked by regions with either top-of-troposphere emissivity or cloud optical thickness above a certain threshold, and found significantly larger trends for severe storms. Furthermore, [Matthee and Mecikalski \(2013\)](#) concluded that most of the investigated infrared fields and their time trends describing updraft strength, cloud depth, and glaciation are significantly different between the nonlightning and lightning-producing convective clouds. [Rosenfeld et al. \(2008\)](#) used a statistical approach to link the vertical cloud-microphysical structure to the potential of severe-storm development. They discussed relations between effective radius of liquid cloud droplets and infrared brightness temperature of an ensemble of growing cumuli and showed that deep clouds composed of small drops in their lower parts and cool bases are more likely to produce hail.

The growth phase of deep convective clouds and its relation to cloud properties in the later mature phase and associated weather phenomena have been most extensively investigated in the United States, whereas less is known for the European continent. In this study, we therefore focus on central Europe with the goal being to investigate the growth phase with regard to 1) thermal cloud-top properties and their changes like infrared brightness temperature and cloud-top cooling rates and 2) cloud optical properties and their changes like cloud optical thickness and effective radius. Even though the small number of cases in this study does not allow a robust attribution of statistical relations, we try to establish a connection between vertical cloud growth and horizontal anvil development derived from satellite imagery. From a collection of very different severe storms, we develop a method not only to quantify the satellite-derived cloud-top properties and their changes but also to make reliable uncertainty estimates for them. The data and methods are described in [section 2](#). After that, the environmental conditions of the cases and occurring weather phenomena are discussed in [section 3](#). Life cycles and the interrelations between satellite-based cloud-top properties are presented in [section 4](#), and conclusions and a summary are given in [section 5](#).

2. Data and methods

a. Satellite data and products

Data from the Spinning Enhanced Visible and Infrared Imager (SEVIRI) have been used in this study,

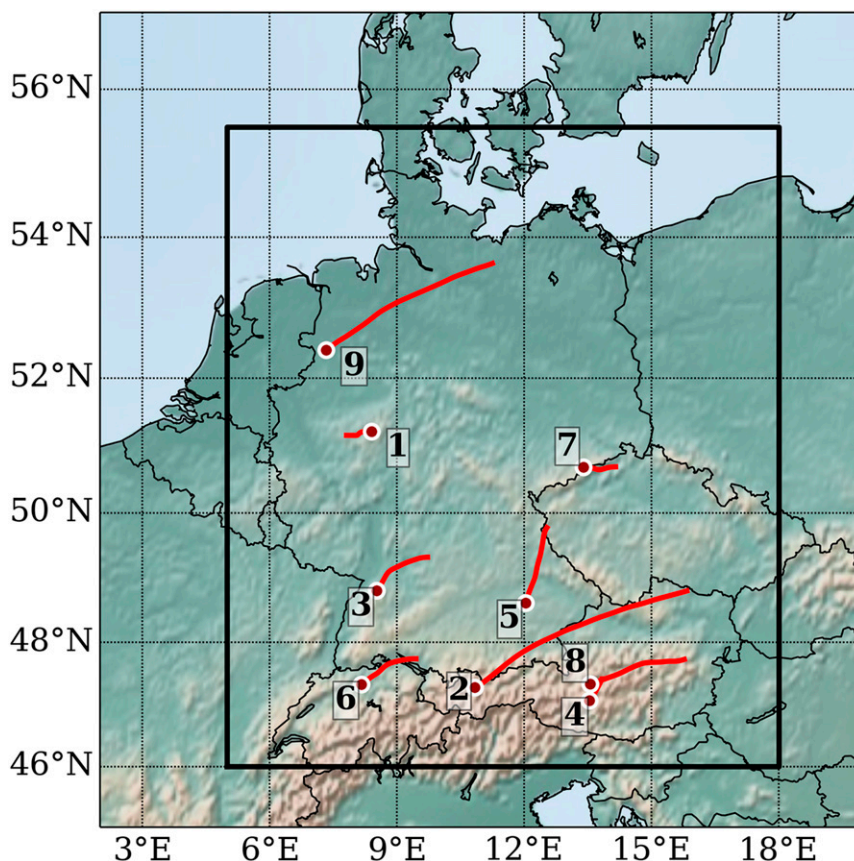


FIG. 1. Overview of the investigated cases. The domain of interest is marked by a black box. In addition, cloud tracks for all investigated cases are plotted (red lines); red circles with white edges indicate the track starting position.

which is the optical imaging radiometer aboard the geostationary Meteosat Second Generation (MSG) satellites operated by EUMETSAT (Schmetz et al. 2002). In the year 2012, which was selected for the case study, *Meteosat-8* performed the so-called rapid-scan service covering Europe with a 5-min repeat cycle. The high temporal resolution enables us to resolve finer details in the convective development as compared with information contained in operational scans with repeat cycles of 15 min. *Meteosat-8* was located at 9.5°E longitude and 0° latitude. In the center of our domain of interest, which covers Germany and parts of western and central Europe (Fig. 1), the infrared image pixel size is 3.2 km in the eastward direction and 6.1 km in the northward direction. Within the marked region, the pixel area varies from approximately 17 km² in the south to 25 km² in the north because of an increased viewing angle.

For tracking and characterization of storms, 3 of 12 SEVIRI channels have mainly been used, the infrared channels at 6.2 and 10.8 μm and the high-resolution visible (HRV) channel. In previous studies, the HRV channel has been found to contain valuable information for identifying deep convective clouds, because they are

often characterized by high reflectances and significant small-scale variability that cannot be resolved by SEVIRI's lower-resolution narrowband channels (Carabajal Henken et al. 2011). The 10.8- μm brightness temperature (BT10.8) is relatively unaffected by emission from atmospheric gases and represents the temperature of the top part of a cloud, the surface, or a mixture of both. In contrast, the water vapor channel at 6.2 μm is very sensitive to water vapor emission in the upper troposphere. A cloud signal appears only for geometrically high clouds. The channel difference between the 6.2- and 10.8- μm channels (BTD) can be used as a measure of distance between the cloud top and the upper-tropospheric water vapor layer that primarily contributes to the outgoing infrared radiation. The BTD is usually negative until deep convective clouds reach their maximum vertical extent at the tropopause level where the BTD changes its sign and is then mainly influenced by water vapor above the cloud (Schmetz et al. 1997). In investigations of convective initiation, the BTD was successfully used as an indicator for vertical cloud depth (see Matthee and Mecikalski 2013, and references therein).

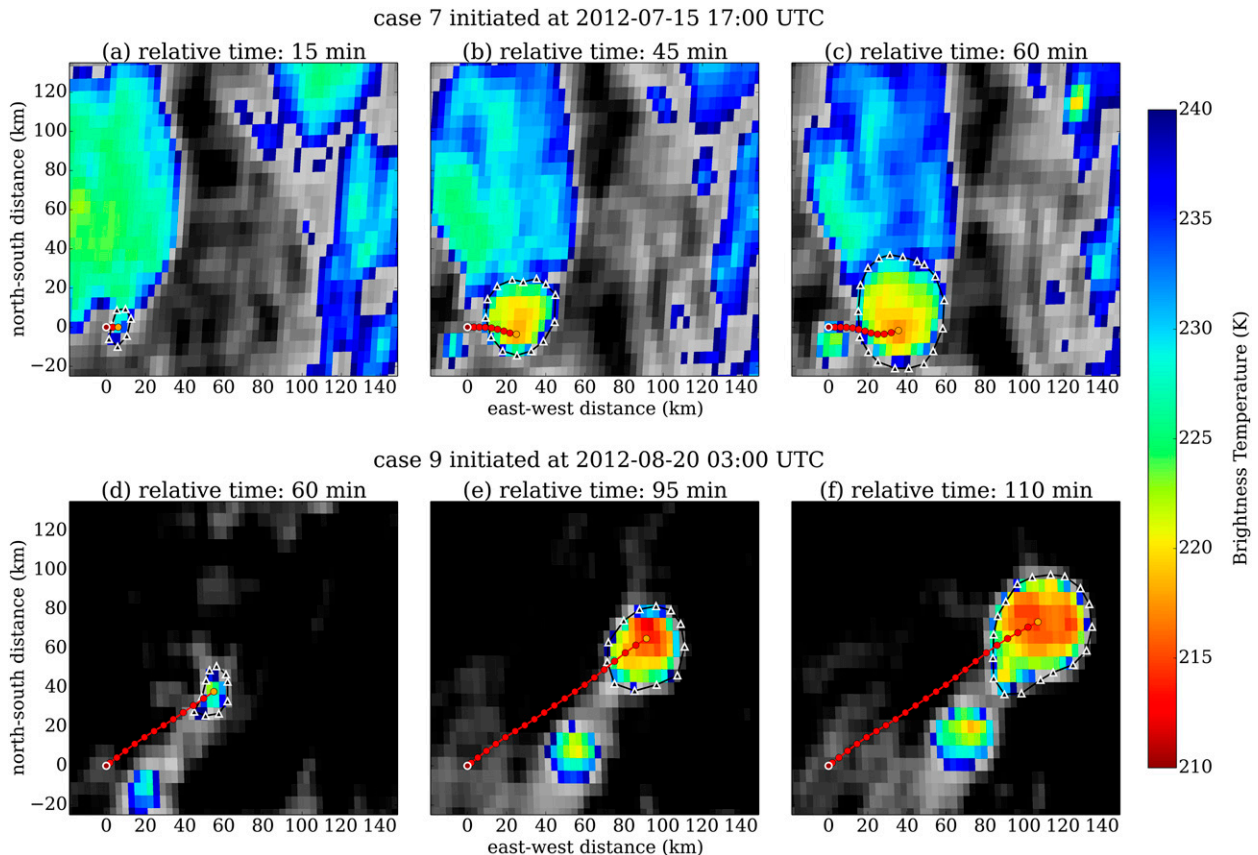


FIG. 2. Evolution of two selected storms shown at three distinct times: (a),(d) time of maximum CTC rate; (b),(e) time of maturity; (c),(f) time at which the cloud anvil reaches a size with equivalent diameter of 50 km. Times and distances are given relative to the track starting position. Red circles mark a smoothed representation of the previous track, the initial starting position is highlighted by a white edge, and the current track position is colored orange. The subjectively determined anvil contour is given by black triangles with white edges. The background image is derived from the $10.8\text{-}\mu\text{m}$ BT, where BTs of greater than 240 K are shown in gray shadings with darker gray values corresponding to warmer BTs and BTs below 240 K are plotted with colors changing from blue to red for decreasing BTs.

For further analysis, the EUMETSAT Satellite Application Facility on Support to Nowcasting and Very Short Range Forecasting cloud-mask product was used to discriminate between cloudy and clear-sky pixels (Derrien and Le Gléau 2005). For cloud-contaminated and cloud-filled pixels, the KNMI cloud physical properties (CPP) algorithm (Roebeling et al. 2006; Meirink et al. 2010) has been applied to retrieve the cloud optical thickness, the cloud phase, and the cloud-top effective radius. The CPP algorithm has been developed and validated within the scope of the Satellite Application Facility on Climate Monitoring (Schulz et al. 2009). It applies a Nakajima–King-type method (Nakajima and King 1990), in which the reflectance of clouds at a nonabsorbing wavelength in the visible spectrum is mainly related to the optical thickness and has small dependence on particle size, whereas the reflectance of clouds at an absorbing wavelength in the near-infrared spectrum is primarily related to particle size. The cloud-phase determination is

done simultaneously, and only the effective radius of ice particles is analyzed in the following. Because retrieved cloud properties are very sensitive to small-scale variability, which is typical for deep convective clouds, large uncertainties are expected (Marshak et al. 2006; Wolters et al. 2010), and retrieval results are interpreted here only in a qualitative manner.

b. Tracking and tracking uncertainty

Storm tracks were manually constructed by following the evolution of BT10.8 features in subsequent images. The starting point of the track corresponds to the location of the initial updraft region, which often coincides with a local minimum of BT10.8. For extending the tracks into the very early stage of cumulus development, where the contrast in the infrared images is low, the high-resolution visible channel was used for cloud identification. All tracks and their initial starting locations are shown in Fig. 1. Furthermore, Fig. 2 shows two examples of storm

tracks combined with the BT10.8 field close to the tracks at three distinct times in the cloud life cycle.

A quantitative uncertainty estimate of along-track storm properties is of interest. Besides resolution limitations as well as measurement and retrieval errors, the tracking accuracy is one crucial factor. Large deviations, especially in derived time trends, are expected if the tracking path jumps from inside to outside the major updraft core and back. A bootstrapping method was applied to quantify the influence of tracking uncertainty on the along-track storm-parameter uncertainty. We assume that the manually determined track is misplaced because of ambiguities in subsequent images but is sufficiently accurate that only one-pixel displacements to the nearest neighbors and the diagonal pixels are considered. Therefore, a region of 3×3 pixels that is centered on the track location contains all possible locations of a misplaced track. For the bootstrapping procedure, a set of random tracks was computed by randomly choosing new track positions out of the original 3×3 pixel region. Storm properties such as BT10.8 were recorded on each random track, and corresponding time trends were calculated. Note that there are just nine different values at each time step but that there are 81 possible trends because of different combinations that were randomly drawn with equal weight. The bootstrapping procedure was repeated 10 000 times, and parameter uncertainties were derived from the interquartile range of the resulting distributions. Note that this estimate of uncertainty does not include the inherent uncertainties of the underlying datasets, which have been discussed previously. In particular, the effects of small-scale variability will add additional errors, on top of the estimates provided by our bootstrapping, that were not considered here.

c. Calculation of cloud-top cooling and anvil expansion rates

The BT10.8 images were centered on the track, stacked in time, and then smoothed in space and time with a Gaussian kernel of two pixels, one pixel, and 5-min width in their respective field dimensions. Because the name “cloud-top cooling” already implies a negative change in cloud-top temperature, the CTC rate is defined here as a negative 5-min trend of BT10.8 along each track, with positive values indicating a decrease in BT10.8. CTC rates were calculated using centered differences. For example, the difference between the BT10.8 values at relative times of 5 and 10 min is divided by 5 min to obtain a CTC rate that is valid at a relative time of 7.5 min, and so forth. Note that the CTC rates presented below were rescaled to values in degrees Celsius per 15 minutes to ease comparison with existing

literature (Mecikalski et al. 2010a,b; Sieglaff et al. 2011), even if a time step of 5 min was used in our calculation. CTC rates are also calculated for the random-track ensemble, and the median CTC rates, which are mainly reported in the following, represent a statistically robust estimate of the cooling trends of cloud tops in a domain of approximately 200 km^2 .

As shown later, CTC rates as a function of time often resemble a hump, with a distinct maximum in the CTC rate. Cloud clusters with their top in the midtroposphere have the fastest vertical upward motion at the time of maximum CTC rate. To estimate the size and width of that CTC hump, a Gaussian function is fitted to the values of CTC rate. Typical properties that emerge from the fit are 1) the magnitude of CTC maximum, 2) the time t_{cool} of the CTC maximum, and 3) the duration Δt_{cool} of the initial cooling event. The latter is calculated from the full width at half maximum values of the Gaussian fit. The Gaussian fit is essential to our analysis and is based on the assumption that the monitored convective growth has a distinct start, end, and centered maximum in the middle. The values derived from the fit are more robust and allow for a better quantification of uncertainties than do values derived from the raw CTC data. An advantage is that integral properties of the convective growth like the total change in cloud-top temperature and the cooling duration are connected with the maximum of cloud-top cooling rate derived from the Gaussian fit. In addition, the sensitivity to noise is reduced.

A least squares nonlinear fit was applied to the along-track values of CTC rates and also to CTC rates of each of the random tracks in the bootstrapping sample. Only those least squares fits for which the relative variance of the resulting residuals was lower than 25% were declared successful and were retained. Note that the functional dependence of the random-track CTC rates might deviate significantly from Gaussian shape. From all successful fits, median as well as lower- and upper-quartile values for each parameter were derived.

Contours of the cirrus anvils are also shown in Fig. 2. They were manually determined from BT10.8 images in which color enhancement for BTs lower than 240 K was chosen. For single-cell storms with sufficient distance to neighboring cells, object contours correspond to the 240-K isoline of BT10.8. For cases in which storms develop out of preexisting deep cloud systems (e.g., see Figs. 2 a–c) and in which splitting or merging with other cells occurs, object contours have been adjusted subjectively. They were selected to give a smooth and physically consistent evolution of only that part of the anvil that could be connected to the investigated updraft. The complex splitting and merging behavior of most of the investigated

TABLE 1. Overview of cases: Time of occurrence, storm type, and thermodynamic and dynamic environmental conditions. The 3–8-km average midtropospheric wind speed, the low-level wind shear magnitude, and the average storm motion speed are denoted by \bar{U} , ΔU , and V , respectively. Severe-weather phenomena extracted from the ESWD and associated with considered cases are heavy rain (R), large hail (H), damaging lightning (L), and severe wind gusts (G).

| No. | Date | Time (UTC) | Type | ML-CAPE (J kg ⁻¹) | θ_e (K) | CTC rates [°C (15 min) ⁻¹] | \bar{U} (m s ⁻¹) | ΔU (m s ⁻¹) | V (m s ⁻¹) | Severe weather |
|-----|-------------|------------|------------|----------------------------------|-------------------|---|-----------------------------------|------------------------------------|-----------------------------|-------------------|
| 1 | 23 May 2012 | 0830–1130 | MCS | 1249 | 330 | 16.6 | 6.0 | 5.3 | 4.2 | R, H, L, G |
| 2 | 8 Jun 2012 | 1310–1800 | MCS | 747 | 332 | 13.8 | 25.1 | 6.6 | 23.9 | R, H, G |
| 3 | 30 Jun 2012 | 1345–1615 | Supercell | 2323 | 348 | 18.4 | 24.9 | 6.9 | 13.4 | H |
| 4 | 3 Jul 2012 | 1100–1230 | Frontal | 2663 | 348 | 17.9 | 15.3 | 7.6 | 9.2 | R, H |
| 5 | 3 Jul 2012 | 0925–1155 | Frontal | 761 | 335 | 8.9 | 15.8 | 3.6 | 16.0 | |
| 6 | 10 Jul 2012 | 1215–1425 | Frontal | 977 | 331 | 13.6 | 21.8 | 4.9 | 14.9 | |
| 7 | 15 Jul 2012 | 1645–1830 | Orographic | 954 | 320 | 15.9 | 12.3 | 5.9 | 11.3 | |
| 8 | 20 Jul 2012 | 1400–1700 | Super cell | 1918 | 342 | 9.8 | 22.3 | 6.8 | 16.9 | R, H, G |
| 9 | 20 Aug 2012 | 0300–0720 | MCS | 3204 | 349 | 11.7 | 20.0 | 7.9 | 20.0 | H, L, G |

storms made it impossible to use automated anvil-tracking routines without the loss of causal relationship between cloud-top vertical velocity and anvil expansion. From the anvil area, the equivalent diameter, which is the diameter of a hypothetical circle with equal area, and the corresponding equivalent radius were calculated. The trend in the equivalent anvil radius is an approximation of the average apparent outward-pointing velocity of the anvil edge (abbreviated anvil edge velocity in the following). It was also determined via centered differences. A Gaussian filter with a kernel width of 15 min was applied to reduce noise in the anvil edge velocity. The running-average deviation between the original and the smoothed values was used to estimate the uncertainty in the trend of equivalent anvil radius at different times.

d. NWP data and environmental parameters

Forecast data from the convection-permitting operational version of the Consortium for Small Scale Modelling (COSMO) numerical weather prediction model (COSMO-DE; Baldauf et al. 2011) have been used for the characterization of the environmental conditions and the flow regime in which the investigated cases formed. COSMO-DE is the operational forecast model of the German Weather Service, with a horizontal resolution of 2.8×2.8 km² and covering a similar domain to that in Fig. 1. It is initialized every 3 h, and data are available from the archive on an hourly basis.

Data values within a distance of 100 km or less from each track's starting point and from 3 h before initiation until the initiation time were taken into consideration. Maximum values of mixed-layer convective available potential energy (ML-CAPE) and low-level equivalent potential temperature were recorded. Furthermore, average low-level wind shear (from ground level up to 1 km) and average midtropospheric wind speeds (from 3 to 8 km) were calculated and were utilized to characterize the storm environment.

3. Environmental conditions of cases

The year 2012 was chosen for a case study of convective storms in the domain of central Europe shown in Fig. 1. Nine cases of developing storms were selected that evolved in different environmental conditions between late May and late August of 2012. An overview of the timing and environmental conditions of the storms is given in Table 1. We remind the reader again that this small number of cases does not allow for a derivation of statistically significant relations between observed dynamical and microphysical properties.

In central Europe, a typical storm environment becomes established when warm, moist marine air is transported along the forward flank of a low pressure area situated at the British Islands or nearby (Wapler and James 2015). Depending on the direct location of the low pressure system, the moist air comes from a westerly direction (cases 2, 7, 8, 9), a southwesterly direction (cases 3 and 6), or a southerly direction (cases 4 and 5). The additional synoptic-scale lift can lead to a massive release of convective energy. In one exceptional case, a large mesoscale convective system (MCS) developed under conditions of northeasterly flow after the passage of a low pressure system that brought moist air from the Mediterranean Sea to northern Germany; the air mass then heated up and further destabilized (case 1). Two other MCSs (cases 2 and 9) were identified by their anvil size. The equivalent anvil diameter exceeded 200 km, which falls approximately into the European MCS classes discussed in Morel and Senesi (2002). Furthermore, two supercells (cases 3 and 8) were reported in the media by storm chasers. The existence of a mesocyclone was verified with available photographs from eyewitnesses. Other cases are connected to lifting along frontal convergence lines (cases 4, 5, and 6) and orographic lifting (case 7).

Storm clouds developed from preexisting cloud fields in eight of nine cases. In cases 3 and 4, prestorm cumuli

formed horizontal structures that were aligned with the mean cloud motion. Hence, storm formation might be connected to the intersection of horizontal rolls and other mesoscale features like local convergence lines (Markowski and Richardson 2010). Cases 5 and 8 evolved out of unstructured cloud fields. In cases 2, 6, and 7, deep convection was triggered at the edge of preexisting mature convective systems, which might be connected to the cold-air outflow of neighboring cold pools. The storm initiation took place mainly on the southern flank of the westward- to northwestward-moving systems. Only for case 1 did the storm-preceding cumuli develop from clear sky.

Severe-weather reports for each of the cases were extracted from the European Severe Weather Database (ESWD; Dotzek et al. 2009). Considered severe-weather categories include heavy rain and flooding (R), large hail (H), damaging lightning (L), and severe wind gusts (G). Large hail is achieved for hailstones larger than 2 cm, and severe wind gusts are defined as straight-line winds with maximal wind speeds greater than 25 m s^{-1} . Some thermodynamic parameters are shown in Table 1 together with maximum CTC rates and reported severe weather. In four cases, values of ML-CAPE were forecast to be close to or greater than 2000 J kg^{-1} in the proximity of convection initiation. In addition, the low-level equivalent potential temperature was predicted to be greater than 340 K for these cases, indicating the transport of warm and moist marine air masses as the origin of potential instability. All cases of high ML-CAPE were accompanied by severe weather in at least one of the four categories mentioned above. Of interest is that there is no systematic relationship between maximum CTC rates and CAPE, which also reflects the complexity of initiation mechanisms over European terrain. In Table 1, some dynamical conditions are presented as well. The average speed of the storm cell derived from manual tracking is generally connected to the mean midtropospheric wind such that for larger wind speeds faster storm motion is achieved. The low-level wind shear between the surface and 1-km altitude is between 4 and 8 m s^{-1} , which is consistent with reported bulk 1-km shear of severe storms in the United States but is much less than values gathered for tornadic storms (Craven and Brooks 2004).

4. Storm development

In the following sections, the results of the storm-cell tracking are discussed. It is shown how a typical life cycle of growing storms is extracted and how several satellite-derived cloud properties—cloud-top temperatures, cloud-top cooling rates, anvil expansion, and changes in effective radius and optical thickness—can be combined

to form an overall picture of the early development of severe convection.

a. Schematic view of storm growth phase

One essential challenge for the comparison of tracks of different storms in different environmental conditions is the method used for their temporal synchronization. Therefore we introduce an idealized model of storm growth as shown in Fig. 3: low-level cumuli grow vertically in one dominant continuous cooling period into a mature cumulonimbus cloud. Vertical growth induces a cooling of the cloud top, with maximum cooling rates reached in the mid- to upper troposphere, and the vertical development stops at the tropopause region. From this picture, we derive essentially three different times: 1) the track initiation time $t_{\text{init}} = 0$, 2) the time t_{cool} at which the cooling reaches its maximum, and 3) the time at which the vertical growth has slowed down, the cumulonimbus cloud has reached its maximum vertical extent, and a transition to horizontal anvil expansion occurs. The latter time marks the transition between growth and mature phase and is termed time of maturity t_{mature} in the following discussion. The time of maturity will be defined later, in section 4c, on the basis of the time trend of the brightness temperature difference between the 6.2- and 10.8- μm SEVIRI channels.

Besides environmental conditions, the detection of storm initiation from satellite relies also on visibility. Especially if a convective tower develops in or at the edge of a preexisting deep convective system, the first detection is only possible if the contrast between the old and the newly developed cell is sufficiently strong. Thus the track starting time t_{init} essentially depends on these shortcomings and is therefore not a suitable property of the developing storm itself in our analysis. Therefore, we use the time of the maximum CTC rate t_{cool} , which marks more objectively a common state of a developing storm and splits the growth phase with the total period of $\Delta t_{\text{growth}} = t_{\text{mature}} - t_{\text{init}}$ into an early updraft intensification period $\Delta t_{\text{before}} = t_{\text{cool}} - t_{\text{init}}$ before t_{cool} and a continued growth-to-maturity period $\Delta t_{\text{after}} = t_{\text{mature}} - t_{\text{cool}}$ after t_{cool} . In addition, a cooling period Δt_{cool} is defined that refers to the time period in which the CTC rates of the developing storms are greater than one-half of the maximum CTC value attained at t_{cool} .

b. Cloud-top cooling rates and vertical motion

The temporal evolution of BT10.8 and CTC rates defined as the 5-min trend of BT10.8 is shown for two examples in Fig. 4. The two selected cases have relatively low and relatively high maximum CTC rates, respectively, with respect to all nine cases. In line with the schematic view discussed above, the magnitude of the CTC rate

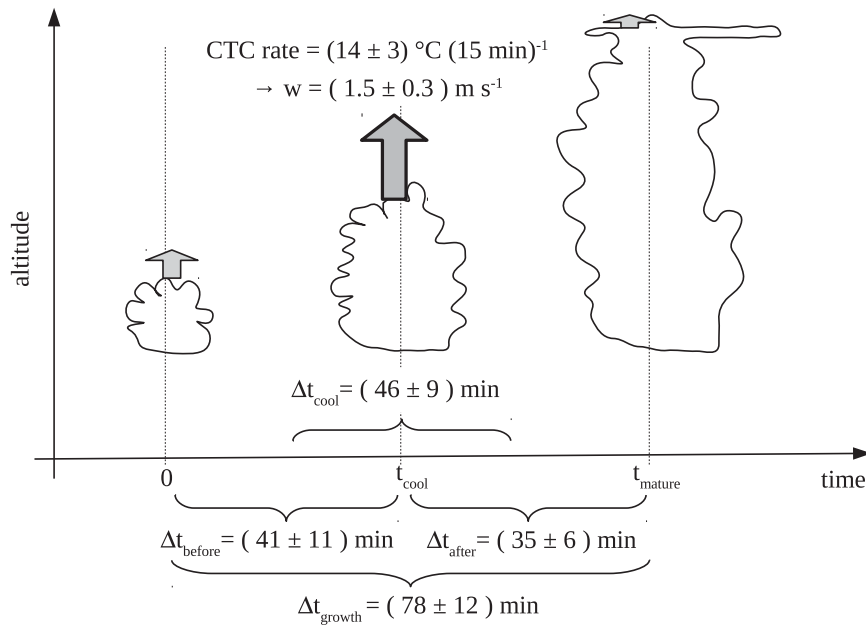


FIG. 3. Sketch of simplified cloud development. Arrows mark cloud-top vertical motion. The times t_{cool} and t_{mature} and the periods Δt_{growth} , Δt_{cool} , Δt_{before} , and Δt_{after} are indicated. Given values represent the respective medians over all cases and the uncertainty intervals as obtained from the cross-case interquartile range.

typically increases during the early development of a storm cell, reaches a distinct maximum, and then decreases again until the storm reaches the mature phase. In 6 of 9 cases of developing storms, we identified only one single dominant maximum in the along-track CTC

rates. In the other cases, a secondary maximum occurred before or after the main maximum (not shown). The median, the interquartile range, and the total minimum–maximum range derived from random-track bootstrapping are also given in Fig. 4. The along-track BT10.8 is mainly

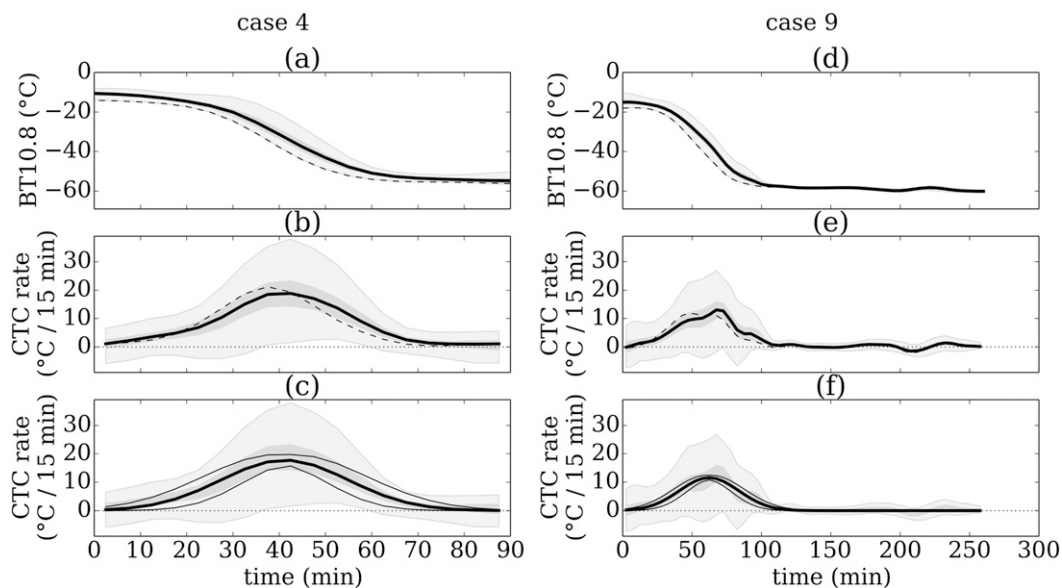


FIG. 4. CTC rate and BT10.8 along track (thin dashed line) for (a)–(c) case 4 and (d)–(f) case 9. From random-track bootstrapping, the minimum–maximum interval (shaded light gray), the interquartile interval (shaded darker gray), and the median (thick solid line) are shown. Results of the Gaussian fits are overlaid on (c) and (f).

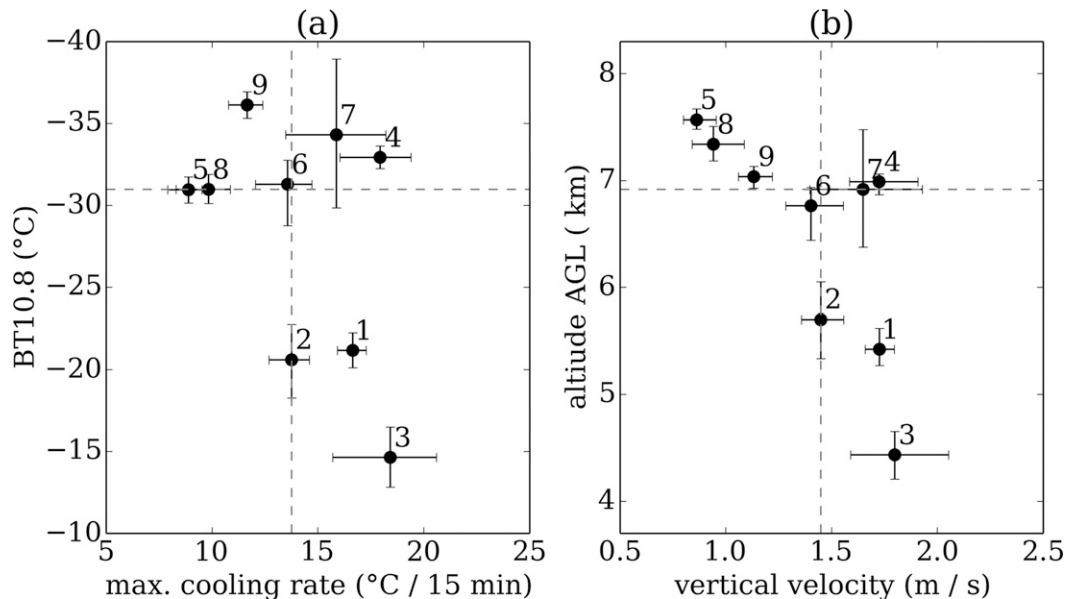


FIG. 5. Relations between (a) BT10.8 and CTC rate and between (b) altitude AGL and vertical velocity at the time when the CTC rate has its maximum value. Circles represent the median values, and error bars represent the interquartile range derived by random-track bootstrapping.

close to the minimum BT10.8 of the 3×3 pixel region, because this is the location where the initial updraft is expected (Adler and Mack 1986). The CTC rate derived along the track remains close to the median of the random-track CTC rates. A shift in timing and magnitude of the maximum in CTC rate is visible for case 4. No systematic differences between the median CTC rate and the along-track CTC rate are evident in the other example, case 9. The Gaussian fit to the CTC rates is also given in Fig. 4. The central curve was constructed from median parameter values; the outer curves show the minimum–maximum interval resulting from any combination of fit parameters in the interquartile range. The median fit curve essentially follows the median CTC rate at the time of the dominant initial cloud growth. The uncertainty interval of possible fits overlaps very well with the interquartile range of the random-track sample.

In Fig. 5a, the relation between the maximum CTC rate and the corresponding BT10.8 value at which the maximum CTC rate appeared is shown. Values and error bars correspond to the median and interquartile range of the parameters derived by the fitting procedure as described above. The median CTC rate is $\sim 14^{\circ}\text{C} (15 \text{ min})^{-1}$, and the median BT10.8 is approximately -30°C averaged over all cases. In concentrating on the extremes, it is seen that case 3 with the greatest maximum CTC rate of $18^{\circ}\text{C} (15 \text{ min})^{-1}$ peaks at -15°C for BT10.8, whereas case 5 with the lowest maximum CTC rate of $9^{\circ}\text{C} (15 \text{ min})^{-1}$ peaks at -31°C for BT10.8. No other systematic behavior between maximum CTC

rates and BT10.8 values has been identified. The range of observed BT10.8 for 50% of the cases with low CTC magnitudes is from -36° to -21°C , which is very similar to the BTs of the other cases, which range between -34° and -15°C .

In the early development phase, the BT10.8 can be composed of both cloud and ground radiative contributions. Hence, the cooling trend in BT10.8 results from two major effects: 1) from a cooling of the cloud top that results from vertical cloud motion and 2) from an apparent optical thickening of the developing cloud structure. The latter is mainly caused by subpixel variations in cloud optical thickness and an increase in fractional cloud cover. Partial surface contributions in the cloud radiative signature might lead to a slight to moderate increase in the infrared brightness temperature and cannot be separated from the pure cloud signal using satellite imagery alone. Downscaling approaches that use the SEVIRI high-resolution visible channel as presented in Deneke and Roebeling (2010), Bley and Deneke (2013), and Mecikalski et al. (2013a) might, however, improve knowledge about subpixel variations in optical thickness but have not been applied within the current study. Hence, neglecting this effect, the cloud-top vertical motion can be estimated knowing the corresponding temperature profile (Adler and Fenn 1979b). The signal in the $10.8\text{-}\mu\text{m}$ channel is dominated by the temperature of the cumulus cloud top. Nevertheless, overlaying semitransparent cirrus can lead to significantly lower BTs relative to the cloud-top temperatures, thus leading to an overestimation of geometric

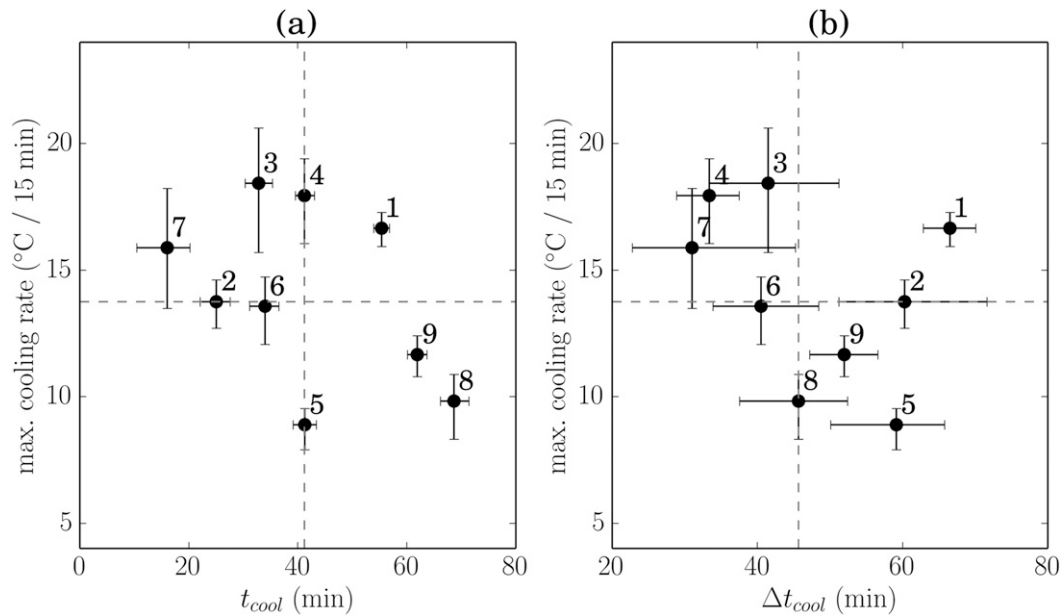


FIG. 6. Relations between (a) timing and maximum CTC rate and between (b) cooling duration and maximum CTC rate. Parameters resulted from a nonlinear least squares fit of a Gauss-shaped curve to each realization of the random-track sample. The width of the Gauss-shaped curve has been converted to the width of one-half of maximum magnitude. Circles represent the median values, and error bars represent the interquartile range.

cloud altitude. For our cases, we excluded by visual analysis the possibility that disturbing cirrus fields were present and move across the convective initiation location. The correct retrieval of cloud properties of growing cumulus beneath cirrus clouds is challenging and is further discussed in [Mecikalski et al. \(2013b\)](#).

Accepting these shortcomings, the BT10.8 are directly interpreted as cloud-top temperatures. Using temperature profiles from the regional weather forecast model COSMO-DE with a $10 \times 10 \text{ km}^2$ region centered on the storm-track location, the cloud-top temperatures are converted to geometric altitude above ground level (AGL) taking also orography into account. The median altitude AGL of maximum cloud-top cooling is $\sim 7 \text{ km}$. More than 50% of the cases achieve their maximum cooling altitude within 6.5–7.5 km AGL. We used a set of temperature profiles in the proximity of the storm track to estimate the uncertainties in the cloud-top temperature-to-altitude conversion. These uncertainties are unimportant relative to vertical shifts resulting from variations in the timing of maximum cloud-top cooling due to tracking uncertainties. Furthermore, additional errors can be introduced by changes in subpixel fractional cloud cover that have not been taken into account. Temperature lapse rates were derived from COSMO-DE and were used to calculate cloud-top vertical motion following the method of [Adler and Fenn \(1979b\)](#) as ratio between CTC rate and temperature lapse rate. In altitudes of maximum CTC, median lapse rates of $-7.6^\circ \text{C km}^{-1}$

were forecast. For the considered cases, the median of maximum vertical velocity of cloud-top motion is $\sim 1.5 \text{ m s}^{-1}$.

In [Fig. 5b](#), the vertical distribution of maximum cloud-top vertical motion is shown. When compared with [Fig. 5a](#), the relation is somewhat clearer but is still very uncertain, with a linear correlation coefficient decreasing from -0.45 to -0.7 . Larger maximum vertical velocities are observed for developing convective storms that have their maximum cooling at a lower altitude above ground. The depicted behavior is similar to that reported by [Adler and Fenn \(1979b\)](#). The magnitude of vertical velocities is much smaller in our study than it is for the vertical velocities of severe storms reported in [Adler and Fenn \(1979b\)](#). This difference might be caused by intrinsic differences between the strength of storms in central Europe and in the United States. Differences in satellite resolution, analysis techniques, and averaging strategies could also be responsible for the large deviations, however.

The relation between the time of the maximum CTC rate t_{cool} , the duration of the cooling Δt_{cool} , and the maximum value of CTC rate derived by the nonlinear least squares fit to a Gaussian curve is given in [Fig. 6](#). The median of the time at which maximum cooling appears is $\sim 40 \text{ min}$, and the median cooling duration is $\sim 45 \text{ min}$. The t_{cool} and the maximum CTC rate exhibit no systematic relation, mainly because the track starting time that influences t_{cool} depends highly on the visibility

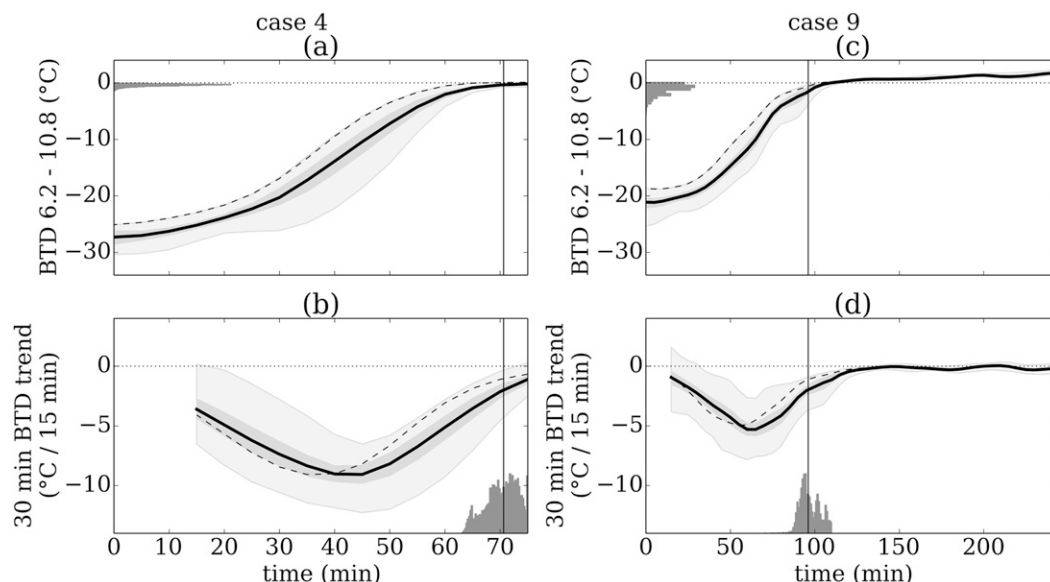


FIG. 7. As in Fig. 4, but for (a),(c) BTD and (b),(d) its corresponding 30-min time trend. Histograms of the estimated time of maturity and the corresponding BTD value are indicated by gray bars at the axis of each plot.

of developing convection. The cooling duration Δt_{cool} and the maximum cooling rate are shown in Fig. 6b. On the one hand, larger maximum CTC rates are expected for shorter cooling periods if the difference between initial and final cloud-top temperature is constant. On the other hand, smaller maximum CTC rates are obtained for smaller total changes in cloud-top temperatures if the cooling period is constant. The spread in data points in Fig. 6b therefore originates from the different total changes in cloud-top temperatures. For all considered cases, initial cloud-top temperatures range from -22° to 15°C . Final cloud-top temperatures vary from -66° to -48°C . With a value of about 12°C , the standard deviation of the initial cloud-top temperatures is more than 2 times as large as that for final cloud-top temperatures.

c. Initial updraft intensification and continued growth

We discussed the distinct growth periods, the initial updraft intensification, and the continued growth period as based on Fig. 3. The time of maturity t_{mature} marks the time at which the initial vertical growth slows significantly down and horizontal expansion of the evolving cloud anvil starts to occur. We will term t_{mature} the end of the total growth phase, even though further cloud-top cooling might be present in the later phase of the thunderstorm, especially when overshooting tops develop. For its determination, the BT difference between the 6.2- and $10.8\text{-}\mu\text{m}$ channels (denoted as BTD in the following) is used in this study. Figure 7 shows the evolution of BTD and its 30-min time trend. Again, along-track values, median, and interquartile range are

indicated for two example cases. We defined the time of storm maturity by the time at which the 30-min BTD time trend crossed a threshold value of $-2^{\circ}\text{C} (15\text{ min})^{-1}$ the first time after the minimum BTD trend. The median BTD at the time of maturity is -2°C . The distribution of t_{mature} and corresponding BTD from random-track ensemble is presented by the histograms in Fig. 7.

The time period Δt_{before} before the maximum CTC rate was compared with the time period Δt_{after} after the maximum CTC rate (not shown). Median of Δt_{after} is ~ 35 min, and essentially all storm cases reach maturity in 30–45 min after the maximum of CTC rates. The spread in Δt_{after} is considerably smaller than that for Δt_{before} . There is no apparent systematic relationship between Δt_{before} and Δt_{after} . That fact makes us suggest that by monitoring the evolution of the CTC rate of a developing storm, it can be expected that the storm reaches maturity 30–45 min after the maximum in cloud-top cooling, independent of its first detection. In Fig. 3, the average duration of the distinct parts of the growth periods is presented. The statistics of the timing of our collection of developing storms are summarized in Fig. 8a. The initial updraft intensification takes on average 41 min, whereas the total growth period persists on average nearly 80 min. The variability in the total growth period originates from variations in the initial updraft intensification period.

d. Anvil expansion rates

In Fig. 9, the evolution of the equivalent anvil diameter, the anvil edge velocity, and the area expansion

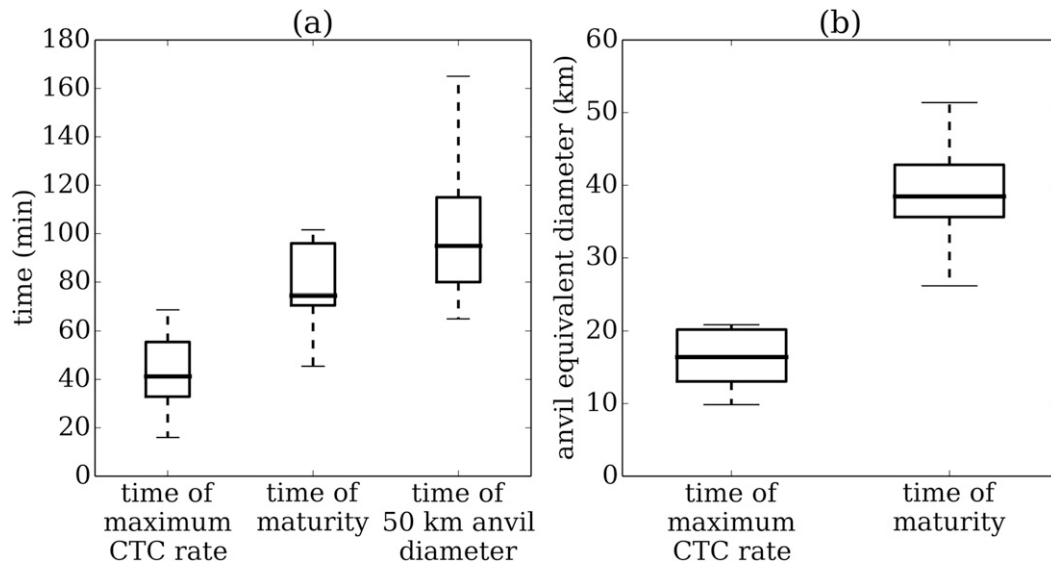


FIG. 8. Box-and-whisker plots of the distribution of (a) times and (b) equivalent anvil diameter at different stages.

rate is presented for cases 3 and 9. The upward-directed mass transport within the updraft core leads to the divergence of the upper-level horizontal flow, causing the satellite-detected anvil area and the corresponding equivalent anvil diameter to increase. Maximal values of anvil edge velocity range from 4 to 12 m s^{-1} . In 5 of 9 cases, the anvil edge velocity remained relatively constant or even increased throughout the first 3 h after

detection. In the other four cases, a nearly linear decrease in time was observed, crossing the zero line after approximately 3 h on average.

The distribution of the equivalent anvil diameter is shown in Fig. 8b at two distinct times. The median anvil diameter at t_{cool} is $\sim 15 \text{ km}$, and it varies roughly between 10 and 20 km. At the time of maturity t_{mature} , however, which is roughly 35 min later, the median anvil

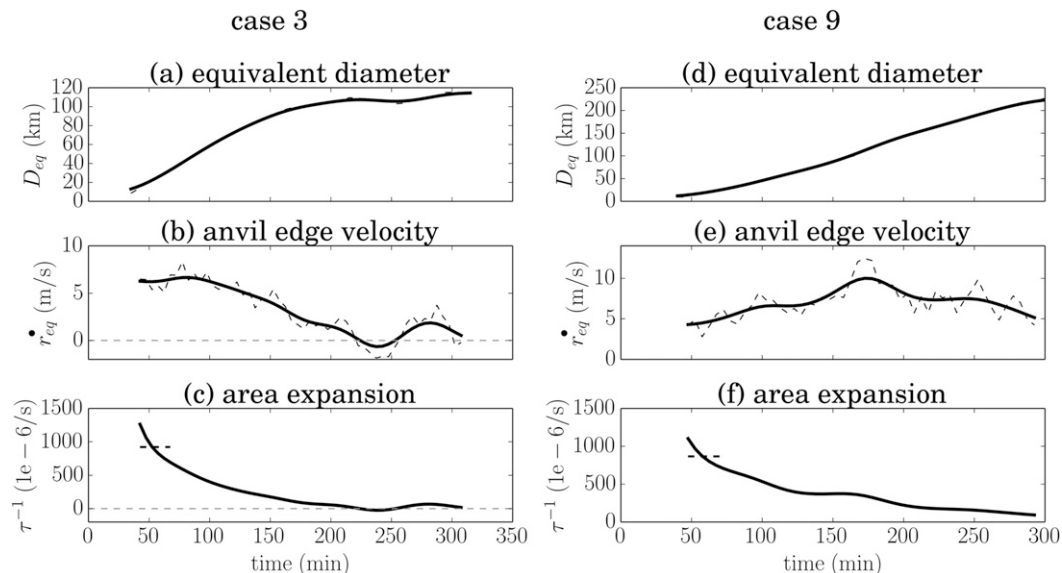


FIG. 9. The temporal evolution of (a),(d) equivalent anvil diameter; (b),(e) anvil edge velocity; and (c),(f) area expansion time rate is shown for (left) case 3 and (right) case 9. The 15-min time trends were calculated by centered difference. Calculated properties (dashed lines) were smoothed with a Gaussian kernel of width 15 min (thick solid line). The darker dashed horizontal line in (c) and (f) is the average area expansion over the first 30 min, as used in Machado and Laurent (2004).

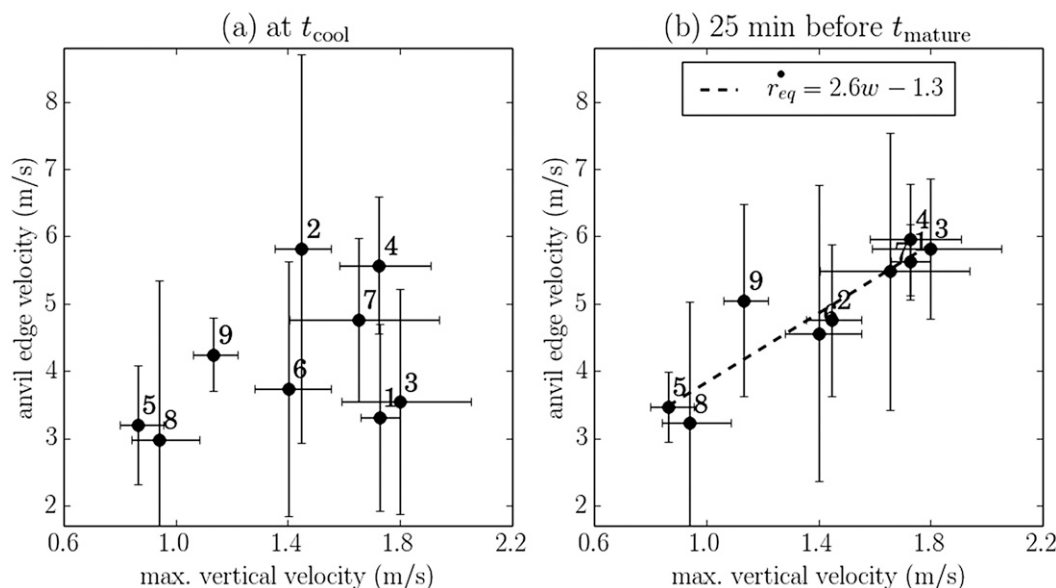


FIG. 10. Relation between maximum vertical velocity and anvil edge velocity relative to two distinct times: (a) time of maximum cooling t_{cool} and (b) 25 min before the time of maturity t_{mature} . Error bars represent the interquartile range estimated from the random-track bootstrapping for CTC rates and from the standard deviation between the temporally filtered and unfiltered radius trends with an averaging interval of 15 min. The dashed line in (b) indicates the least squares regression line between mean values.

diameter has increased to 38 km, with larger variations ranging from 25 to 50 km.

Values of the maximum vertical velocity that are obtained at the time t_{cool} are now compared with the values of the anvil edge velocity at two distinct times, t_{cool} and 25 min before t_{mature} . The corresponding relations are shown in Fig. 10. The upward vertical motion in the updraft core and the outward-pointing horizontal motion in the altitudes of the storm anvil might be connected by the mass transport within the storm cell. At t_{cool} , the storm anvil or the cloud parts that are cold enough to be detected as anvil just start to appear in the satellite imagery. No instantaneous correlation between the vertical motion and anvil edge velocity can be identified (see Fig. 10a), which was expected. We believe that changes in the cloud morphology rather than mass transport dominate the anvil changes at this stage. The apparent changes in anvil size can occur as more and more parts of the cloud complex become colder than the threshold of 240 K to be detected as anvil during the growth stage of the cloud cluster. This effect was described as vertical shift in the sloping isotherms by Adler and Fenn (1979a). Furthermore, local changes in the shape of the cluster can strongly influence the apparent motion of the anvil edge. Later, however, the anvil edge velocity correlates well with the maximum vertical motion detected at t_{cool} , with a linear correlation coefficient of 0.92 between median quantities.

In addition, Fig. 11 shows the linear correlation coefficient between the maximum vertical velocity given at t_{cool} and the anvil edge velocity at different times. Two different synchronization strategies were considered. First, the anvil edge velocity was calculated relative to the time of maximum cloud-top cooling t_{cool} (see Fig. 11a). Second, the anvil edge velocity was computed relative to the time of maturity t_{mature} (see Fig. 11b). Values of greater than 0.85 are highlighted and give the time period in which a connection between cloud-top vertical velocity and horizontal anvil edge velocity is established. High correlations are found for time lags of 20–30 min relative to t_{cool} . A larger time period of 35 min before t_{mature} up to the actual begin of the mature phase is observed for the other synchronization strategy. It is reasonable to believe that a connection between the vertical and horizontal motion builds up after a certain time because of transport of mass within the developing cloud. The decay of correlation seems to be less clear, however. One could speculate that the connection disappears after changes in the updraft strength that cannot be observed by satellite imagery become significant. The involved time scales might reveal interesting insights on the common dynamical behavior of growing storms. A robust quantification of these properties on the basis of a large statistical sample is, however, postponed to future work.

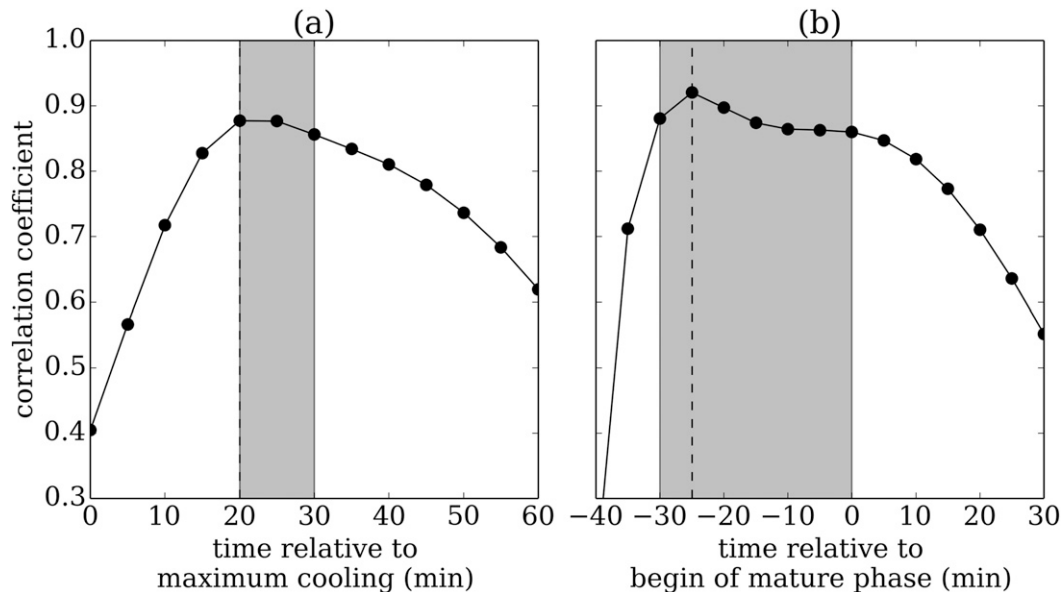


FIG. 11. Linear correlation coefficient between vertical cloud-top motion and horizontal anvil edge velocity for different times relative to (a) the time of maximum CTC and (b) the time of maturity. The gray-shaded regions mark intervals with a linear correlation coefficient of greater than 0.85. The dashed vertical lines mark the times of maximum correlation.

e. Microphysical and optical storm properties

The evolution of cloud ice effective radius and cloud optical thickness was studied during growth of our cases (not shown). These properties exhibit much larger variations than do the earlier-discussed cloud properties. Deep cumulus clouds are often characterized by significant variability in the HRV reflectance, which is not resolved by SEVIRI's low-resolution channels (Carabaja Henken et al. 2011) and is likely caused by cloud regions that are shaded from solar illumination and partly cloud-filled pixels at the cloud edges. Note that this subpixel variability can significantly degrade the accuracy of the retrieved cloud properties (Marshak et al. 2006; Wolters et al. 2010). The cloud ice effective radius varies from 10 to 40 μm . During the initial updraft intensification phase, the cloud phase changes from liquid to ice. In the continued growth phase, the effective radius increases for one-half of the cases and remains constant or decreases slightly for the other half. The cloud optical thickness generally increases during the growth phase and reaches values that are close to the saturation limit at the beginning of the mature phase. Values of the cloud optical thickness above 80–100 are very sensitive to small changes in reflectance and should only be considered in a qualitative sense.

The statistical behavior of the cloud properties of all cases is summarized in box-and-whisker plots in Fig. 12. The median effective radius at the time of maximum

cooling is $\sim 18 \mu\text{m}$ and is slightly larger than the median effective radius at the time of maturity with $16 \mu\text{m}$. The spread in effective radius is very large, and no systematic behavior of the effective radius can be identified. More obvious is that the cloud optical thickness shown in Fig. 12b is increasing during vertical cloud growth. Median values in optical thickness of ~ 25 at t_{cool} increase to median values of ~ 70 at t_{mature} . These values are in line with values reported in several earlier studies. For instance, Hong et al. (2007) found average satellite-derived cloud optical thicknesses to be near or greater than 40 for deep convective clouds, which might correspond to a cumulus stage in the middle of our defined continued growth period. Mecikalski et al. (2011, 2013b) found average temporal changes in optical thickness of 30–50 within 30 min of most intensive convective growth, which is also similar to the changes in optical thickness reported here.

In Fig. 13, the relation between the maximum vertical velocity at t_{cool} and the cloud ice effective radius 25 min before t_{mature} is presented. The linear correlation coefficient is -0.97 , but only six cases have been included because of the retrieval requirement of sufficiently high sun elevation. The observed relationship supports the hypothesis that stronger updrafts in the growth phase lead to smaller ice crystals at the cloud top (Rosenfeld et al. 2008). It is interesting that the largest correlation is observed 25 min before the beginning of the mature phase and suggests a link between the dynamics and the

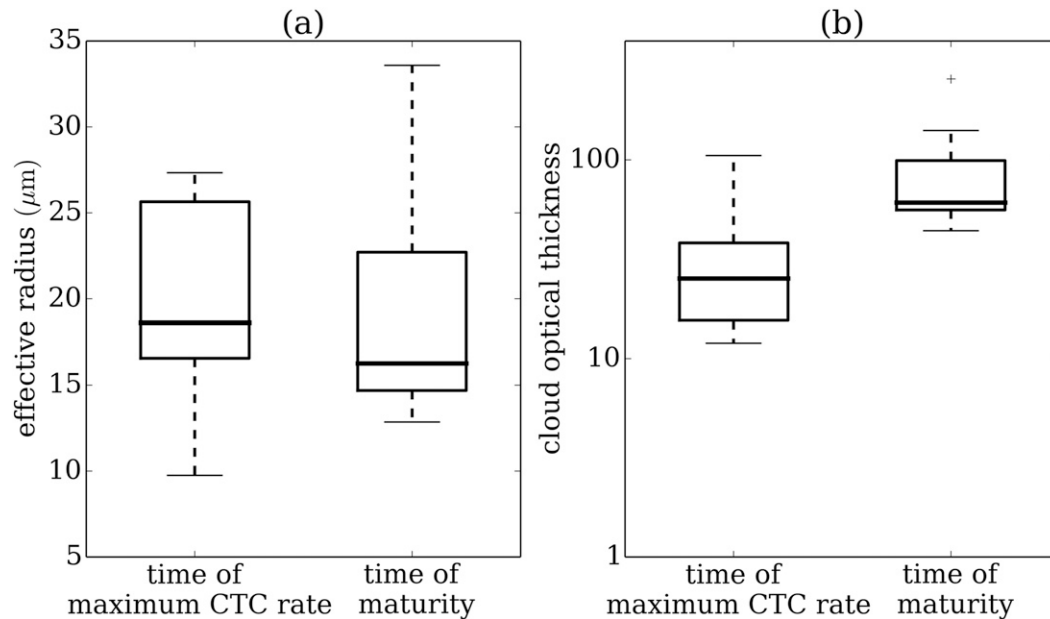


FIG. 12. Box-and-whisker plots of the distribution of (a) cloud ice effective radius and (b) cloud optical thickness at two different stages.

microphysical properties for developing storms, at least for the region of central Europe considered here.

5. Summary and outlook

We studied the early development phase of severe convective storms over central Europe for nine selected cases from 2012. A comprehensive understanding of the growth phase of developing storms has important implications for nowcasting (Roberts and Rutledge 2003; Mecikalski and Bedka 2006; Zinner et al. 2008; Mecikalski et al. 2010a,b; Siewert et al. 2010; Sieglaff et al. 2011; Merk and Zinner 2013; Sieglaff et al. 2014). One of the outstanding strengths of geostationary satellite imagers is their ability to observe convection before the onset of precipitation and lightning. The life cycle of storms as reflected by the temporal changes of several satellite-based storm properties—infrared cloud-top temperature, cloud-top cooling rate, cloud ice effective radius, and cloud optical thickness—was recorded along their tracks. For this purpose, we manually derived the storm tracks from visible and infrared satellite images from the 5-min rapid-scan service of the Meteosat SEVIRI. In addition to satellite observations, data from the COSMO-DE regional forecast model were used to characterize the environmental conditions for convection initiation, and entries from the ESWD were obtained to identify severe-weather phenomena accompanying these storms. Even for manual tracking, ambiguities in satellite images introduced by a still-too-coarse resolution or other reasons

can lead to misplaced tracking paths. We therefore developed a simple method to estimate the uncertainty of along-track storm properties that results from tracking errors.

The majority of the nine studied storms show a distinct maximum in cloud-top cooling rate. The time of the

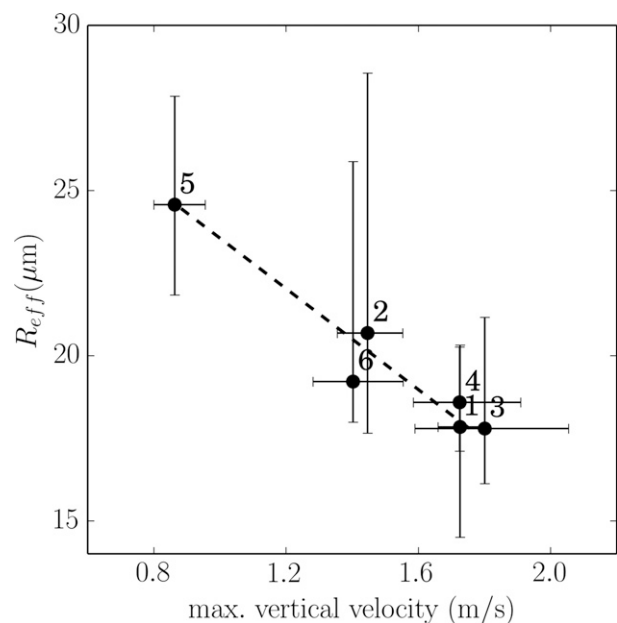


FIG. 13. As in Fig. 10, but for maximum vertical velocity vs cloud ice effective radius at 25 min before the time of maturity. A linear least squares fit between median values is indicated by a dashed line.

maximum cooling was used for synchronization of the storm tracks. The cloud growth phase was divided into an initial updraft intensification period before the maximum cooling and a continued growth period afterward. It was shown that the duration of the initial updraft intensification period varies from 15 to 70 min and strongly depends on the convection initiation mechanism and general visibility conditions. The later continued growth period has a more constant duration and lasts between 30 and 45 min.

Typical maximum cloud-top cooling rates range from 8° to $18^{\circ}\text{C (15 min)}^{-1}$, with uncertainties due to tracking errors being on the order of $1^{\circ}\text{C (15 min)}^{-1}$. The average infrared cloud-top temperature at maximum cooling is approximately -30°C . Relating the cloud-top temperature to the altitude above ground using temperature profiles from COSMO-DE, this corresponds to a maximum cooling height of about 7 km above ground. Using temperature lapse rates from COSMO-DE, the cloud-top cooling rates were converted to average cloud-top vertical velocities with values on the order of a few meters per second. In agreement with Adler and Fenn (1979b), larger cloud-top vertical velocities were found for storms that have their maximum cooling at a lower altitude above the surface. The anvil area and its change were also determined from infrared satellite images. The resulting average anvil edge velocity ranges from 3 to 10 m s^{-1} , with an uncertainty on the order of 2 m s^{-1} . The anvil edge velocity was correlated with the cloud-top vertical velocity, with maximum correlation observed for a time lag of $\sim 20\text{--}30$ min after the maximum in cloud-top cooling rate.

In addition, satellite-retrieved cloud properties were considered along the tracks. Cloud optical thickness and effective radius of cloud ice particles exhibited much larger variations than did the thermal storm properties. The cloud optical thickness is generally increasing during the growth phase, with typical values of 25 during the time of maximum cooling and 70 at end of the growth phase. No systematic behavior in time was identified for the cloud effective radius, but larger effective radii were found for cases with lower vertical growth velocities. The largest anticorrelation with cloud-top vertical velocity was also reached with a delay of 20 min after the maximum cloud-top cooling. We propose that, for larger updraft speeds, ice crystals have less time to grow and hence particles reaching the cloud top will be smaller.

Because the results of this study were based on collection of only nine individual cases, much attention was paid to derive error estimates from the tracking method itself. An increase in the number of investigated storms, to, say, 100 independent cases, will give the possibility of verifying assumptions on the size and statistics of

imposed errors and to check consistency. We expect to converge to a statistically robust average picture of thunderstorm growth and life-cycle properties when the mentioned increase in sample size is pursued. To delineate effects of synoptical patterns, annual cycle, and interannual variability on satellite-detected thunderstorm properties, we think another increase in the number of cases by an order of magnitude is needed—a level that, in our opinion, will mark the limit of manual analysis. It is planned to build up such a large collection of cases in the future and also to combine this collection with information from other sensors, mainly the precipitation data from the German Radar Network and lightning data (Betz et al. 2009). Clustering methods—for instance, as developed in Walker et al. (2012)—can use such a dataset for validation and training of the algorithms and will, after successful implementation, help to build up a fully automated system to further increase sample size.

Acknowledgments. This research was carried out in the Hans Ertel Centre for Weather Research—a cooperative research network of German universities, research institutes, and the German Weather Service that is funded by the BMVBS (Federal Ministry of Transport, Building, and Urban Development). We thank Kathrin Wapler and Daniel Merk for their helpful comments on earlier versions of the manuscript. Furthermore, we thank three anonymous reviewers whose suggestions helped to improve the paper. We acknowledge the work of Martin Rempel, who provided manually determined anvil contours for further analysis.

REFERENCES

- Adler, R. F., and D. D. Fenn, 1979a: Thunderstorm intensity as determined from satellite data. *J. Appl. Meteor.*, **18**, 502–517, doi:[10.1175/1520-0450\(1979\)018<0502:TIADFS>2.0.CO;2](https://doi.org/10.1175/1520-0450(1979)018<0502:TIADFS>2.0.CO;2).
- , and —, 1979b: Thunderstorm vertical velocities estimated from satellite data. *J. Atmos. Sci.*, **36**, 1747–1754, doi:[10.1175/1520-0469\(1979\)036<1747:TVVEFS>2.0.CO;2](https://doi.org/10.1175/1520-0469(1979)036<1747:TVVEFS>2.0.CO;2).
- , and R. A. Mack, 1986: Thunderstorm cloud top dynamics as inferred from satellite observations and a cloud top parcel model. *J. Atmos. Sci.*, **43**, 1945–1960, doi:[10.1175/1520-0469\(1986\)043<1945:TCTDAI>2.0.CO;2](https://doi.org/10.1175/1520-0469(1986)043<1945:TCTDAI>2.0.CO;2).
- Baldauf, M., A. Seifert, J. Förstner, D. Majewski, M. Raschendorfer, and T. Reinhardt, 2011: Operational convective-scale numerical weather prediction with the COSMO Model: Description and sensitivities. *Mon. Wea. Rev.*, **139**, 3887–3905, doi:[10.1175/MWR-D-10-05013.1](https://doi.org/10.1175/MWR-D-10-05013.1).
- Betz, H. D., K. Schmidt, P. Laroche, P. Blanchet, W. P. Oettinger, E. Defer, Z. Dziewit, and J. Konarski, 2009: LINET—An international lightning detection network in Europe. *Atmos. Res.*, **91**, 564–573, doi:[10.1016/j.atmosres.2008.06.012](https://doi.org/10.1016/j.atmosres.2008.06.012).
- Bley, S., and H. Deneke, 2013: A threshold-based cloud mask for the high-resolution visible channel of Meteosat Second Generation

- SEVIRI. *Atmos. Meas. Tech.*, **6**, 2713–2723, doi:[10.5194/amt-6-2713-2013](#).
- Carabajal Henken, C., M. J. Schmeits, H. Deneke, and R. A. Roebeling, 2011: Using MSG-SEVIRI cloud physical properties and weather radar observations for the detection of Cb/TCu clouds. *J. Appl. Meteor. Climatol.*, **50**, 1587–1600, doi:[10.1175/2011JAMC2601.1](#).
- Cintineo, J. L., M. J. Pavolonis, J. M. Sieglaff, and A. K. Heidinger, 2013: Evolution of severe and nonsevere convection inferred from GOES-derived cloud properties. *J. Appl. Meteor. Climatol.*, **52**, 2009–2023, doi:[10.1175/JAMC-D-12-0330.1](#).
- Craven, J. P., and H. E. Brooks, 2004: Baseline climatology of sounding derived parameters associated with deep, moist convection. *Natl. Wea. Dig.*, **28** (1), 13–24.
- Deneke, H. M., and R. A. Roebeling, 2010: Downscaling of METEOSAT SEVIRI 0.6 and 0.8 μm channel radiances utilizing the high-resolution visible channel. *Atmos. Chem. Phys.*, **10**, 9761–9772, doi:[10.5194/acp-10-9761-2010](#).
- Derrien, M., and H. Le Gléau, 2005: MSG/SEVIRI cloud mask and type from SAFNWC. *Int. J. Remote Sens.*, **26**, 4707–4732, doi:[10.1080/01431160500166128](#).
- Dotzek, N., P. Groenemeijer, B. Feuerstein, and A. M. Holzer, 2009: Overview of ESSL's severe convective storms research using the European Severe Weather Database ESWD. *Atmos. Res.*, **93**, 575–586, doi:[10.1016/j.atmosres.2008.10.020](#).
- Heymsfield, G. M., R. H. Blackmer Jr., and S. Schotz, 1983: Upper-level structure of Oklahoma tornadic storms on 2 May 1979. I: Radar and satellite observations. *J. Atmos. Sci.*, **40**, 1740–1755, doi:[10.1175/1520-0469\(1983\)040<1740:ULSOOT>2.0.CO;2](#).
- Hong, G., P. Yang, B.-C. Gao, B. A. Baum, Y. X. Hu, M. D. King, and S. Platnick, 2007: High cloud properties from three years of MODIS Terra and Aqua collection-4 data over the tropics. *J. Appl. Meteor. Climatol.*, **46**, 1840–1856, doi:[10.1175/2007JAMC1583.1](#).
- Machado, L. A. T., and H. Laurent, 2004: The convective system area expansion over Amazonia and its relationships with convective system life duration and high-level wind divergence. *Mon. Wea. Rev.*, **132**, 714–725, doi:[10.1175/1520-0493\(2004\)132<0714:TCSAEO>2.0.CO;2](#).
- , W. B. Rossow, R. L. Guedes, and A. W. Walker, 1998: Life cycle variations of mesoscale convective systems over the Americas. *Mon. Wea. Rev.*, **126**, 1630–1654, doi:[10.1175/1520-0493\(1998\)126<1630:LCVOMC>2.0.CO;2](#).
- Markowski, P., and Y. Richardson, 2010: *Mesoscale Meteorology in Midlatitudes*. Wiley-Blackwell, 418 pp.
- Marshak, A., S. Platnick, T. Varnai, G. Wen, and R. F. Cahalan, 2006: Impact of three-dimensional radiative effects on satellite retrievals of cloud droplet sizes. *J. Geophys. Res.*, **111**, D09207, doi:[10.1029/2005JD006686](#).
- Matthee, R., and J. R. Mecikalski, 2013: Geostationary infrared methods for detecting lightning-producing cumulonimbus clouds. *J. Geophys. Res. Atmos.*, **118**, 6580–6592, doi:[10.1002/jgrd.50485](#).
- McAnelly, R. L., and W. R. Cotton, 1989: The precipitation life cycle of mesoscale convective complexes over the central United States. *Mon. Wea. Rev.*, **117**, 784–808, doi:[10.1175/1520-0493\(1989\)117<0784:TPLCOM>2.0.CO;2](#).
- Mecikalski, J. R., and K. M. Bedka, 2006: Forecasting convective initiation by monitoring the evolution of moving cumulus in daytime GOES imagery. *Mon. Wea. Rev.*, **134**, 49–77, doi:[10.1175/MWR3062.1](#).
- , —, S. J. Paech, and L. A. Litten, 2008: A statistical evaluation of GOES cloud-top properties for nowcasting convective initiation. *Mon. Wea. Rev.*, **136**, 4899–4914, doi:[10.1175/2008MWR2352.1](#).
- , W. M. MacKenzie Jr., M. Koenig, and S. Muller, 2010a: Cloud-top properties of growing cumulus prior to convective initiation as measured by Meteosat Second Generation. Part I: Infrared fields. *J. Appl. Meteor. Climatol.*, **49**, 521–534, doi:[10.1175/2009JAMC2344.1](#).
- , —, —, and —, 2010b: Cloud-top properties of growing cumulus prior to convective initiation as measured by Meteosat Second Generation. Part II: Use of visible reflectance. *J. Appl. Meteor. Climatol.*, **49**, 2544–2558, doi:[10.1175/2010JAMC2480.1](#).
- , P. D. Watts, and M. Koenig, 2011: Use of Meteosat Second Generation optimal cloud analysis fields for understanding physical attributes of growing cumulus clouds. *Atmos. Res.*, **102**, 175–190, doi:[10.1016/j.atmosres.2011.06.023](#).
- , M. König, and C. P. Jewett, 2013a: Application of high-resolution visible sharpening of partly cloudy pixels in Meteosat Second Generation infrared imagery. *Atmos. Res.*, **134**, 1–11, doi:[10.1016/j.atmosres.2013.07.014](#).
- , P. Minnis, and R. Palikonda, 2013b: Use of satellite derived cloud properties to quantify growing cumulus beneath cirrus clouds. *Atmos. Res.*, **120–121**, 192–201, doi:[10.1016/j.atmosres.2012.08.017](#).
- Meirink, J. F., R. Roebeling, E. Wolters, and H. Deneke, 2010: Algorithm theoretical basis document: Cloud physical products—SEVIRI/AVHRR. EUMETSAT Satellite Application Facility on Climate Monitoring Rep. SAF/CM/KNMI/ATBD/CPP, 23 pp. [Available online at http://www.knmi.nl/publications/fulltexts/saf_cm_knmi_atbd_cpp_1.0.pdf.]
- Merk, D., and T. Zinner, 2013: Detection of convective initiation using Meteosat SEVIRI: Implementation in and verification with the tracking and nowcasting algorithm Cb-TRAM. *Atmos. Meas. Tech.*, **6**, 1903–1918, doi:[10.5194/amt-6-1903-2013](#).
- Morel, C., and S. Senesi, 2002: A climatology of mesoscale convective systems over Europe using satellite infrared imagery. I: Methodology. *Quart. J. Roy. Meteor. Soc.*, **128**, 1953–1971, doi:[10.1256/003590002320603485](#).
- Nakajima, T., and M. King, 1990: Determination of the optical thickness and effective particle radius of clouds from reflected solar radiation measurements. Part I: Theory. *J. Atmos. Sci.*, **47**, 1878–1893, doi:[10.1175/1520-0469\(1990\)047<1878:DOTOTA>2.0.CO;2](#).
- Reynolds, D. W., 1980: Observations of damaging hailstorms from geosynchronous satellite digital data. *Mon. Wea. Rev.*, **108**, 337–348, doi:[10.1175/1520-0493\(1980\)108<0337:OODHFG>2.0.CO;2](#).
- Roberts, R., and S. Rutledge, 2003: Nowcasting storm initiation and growth using GOES-8 and WSR-88D data. *Wea. Forecasting*, **18**, 562–584, doi:[10.1175/1520-0434\(2003\)018<0562:NSIAGU>2.0.CO;2](#).
- Roebeling, R. A., A. J. Feijt, and P. Stammes, 2006: Cloud property retrievals for climate monitoring: Implications of differences between Spinning Enhanced Visible and Infrared Imager (SEVIRI) on Meteosat-8 and Advanced Very High Resolution Radiometer (AVHRR) on NOAA-17. *J. Geophys. Res.*, **111**, D20120, doi:[10.1029/2005JD006990](#).
- Rosenfeld, D., W. L. Woodley, A. Lerner, G. Kelman, and D. T. Lindsey, 2008: Satellite detection of severe convective storms by their retrieved vertical profiles of cloud particle effective radius and thermodynamic phase. *J. Geophys. Res.*, **113**, D04208, doi:[10.1029/2007JD008600](#).
- Schmetz, J., S. Tjemkes, M. Gube, and L. van de Berg, 1997: Monitoring deep convection and convective overshooting

- with Meteosat. *Adv. Space Res.*, **19**, 433–441, doi:[10.1016/S0273-1177\(97\)00051-3](https://doi.org/10.1016/S0273-1177(97)00051-3).
- , P. Pili, S. Tjemkes, D. Just, J. Kerkmann, S. Rota, and A. Ratier, 2002: An introduction to Meteosat Second Generation (MSG). *Bull. Amer. Meteor. Soc.*, **83**, 977–992, doi:[10.1175/1520-0477\(2002\)083<0977:AITMSG>2.3.CO;2](https://doi.org/10.1175/1520-0477(2002)083<0977:AITMSG>2.3.CO;2).
- Schmit, T. J., M. M. Gunshor, W. P. Menzel, J. J. Gurka, J. Li, and A. S. Bachmeier, 2005: Introducing the Next-Generation Advanced Baseline Imager on GOES-R. *Bull. Amer. Meteor. Soc.*, **86**, 1079–1096, doi:[10.1175/BAMS-86-8-1079](https://doi.org/10.1175/BAMS-86-8-1079).
- Schulz, J., and Coauthors, 2009: Operational climate monitoring from space: The EUMETSAT Satellite Application Facility on Climate Monitoring (CM-SAF). *Atmos. Chem. Phys.*, **9**, 1687–1709, doi:[10.5194/acp-9-1687-2009](https://doi.org/10.5194/acp-9-1687-2009).
- Sieglaff, J. M., L. M. Counce, W. F. Feltz, K. M. Bedka, M. J. Pavolonis, and A. K. Heidinger, 2011: Nowcasting convective storm initiation using satellite-based box-averaged cloud-top cooling and cloud-type trends. *J. Appl. Meteor. Climatol.*, **50**, 110–126, doi:[10.1175/2010JAMC2496.1](https://doi.org/10.1175/2010JAMC2496.1).
- , —, and —, 2014: Improving satellite-based convective cloud growth monitoring with visible optical depth retrievals. *J. Appl. Meteor. Climatol.*, **53**, 506–520, doi:[10.1175/JAMC-D-13-0139.1](https://doi.org/10.1175/JAMC-D-13-0139.1).
- Siewert, C. W., M. Koenig, and J. R. Mecikalski, 2010: Application of Meteosat Second Generation data towards improving the nowcasting of convective initiation. *Meteor. Appl.*, **17**, 442–451, doi:[10.1002/met.176](https://doi.org/10.1002/met.176).
- Walker, J. R., W. M. MacKenzie Jr., J. R. Mecikalski, and C. P. Jewett, 2012: An enhanced geostationary satellite-based convective initiation algorithm for 0–2-h nowcasting with object tracking. *J. Appl. Meteor. Climatol.*, **51**, 1931–1949, doi:[10.1175/JAMC-D-11-0246.1](https://doi.org/10.1175/JAMC-D-11-0246.1).
- Wapler, K., and P. James, 2015: Thunderstorm occurrence and characteristics in central Europe under different synoptic conditions. *Atmos. Res.*, doi:[10.1016/j.atmosres.2014.07.011](https://doi.org/10.1016/j.atmosres.2014.07.011), in press.
- Wolters, E. L. A., H. M. Deneke, B. J. J. M. van den Hurk, J. F. Meirink, and R. A. Roebeling, 2010: Broken and inhomogeneous cloud impact on satellite cloud particle effective radius and cloud-phase retrievals. *J. Geophys. Res.*, **115**, D10214, doi:[10.1029/2009JD012205](https://doi.org/10.1029/2009JD012205).
- Zinner, T., H. Mannstein, and A. Tafferner, 2008: Cb-TRAM: Tracking and monitoring severe convection from onset over rapid development to mature phase using multi-channel Meteosat-8 SEVIRI data. *Meteor. Atmos. Phys.*, **101**, 191–210, doi:[10.1007/s00703-008-0290-y](https://doi.org/10.1007/s00703-008-0290-y).